Aquatic Toxicology 258 (2023) 106496

Contents lists available at ScienceDirect

Aquatic Toxicology

journal homepage: www.elsevier.com/locate/aqtox

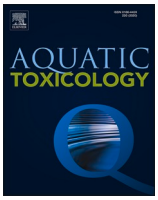

Effect of mercury in the influx and efflux of nutrients in the microalga *Desmodesmus armatus*

Catalina Quevedo-Ospina [a,*], Catalina Arroyave [b], Mariana Peñuela-Vásquez [a], Adriana Villegas [c]

[a] Bioprocess Research Group, Department of Chemical Engineering, Faculty of Engineering, Universidad de Antioquia UdeA, Calle 70 No. 52-21, Medellín 050010, Colombia
[b] GRINBIO Research Group, Department of Environmental Engineering, Universidad de Medellín UdeM, Carrera 87 #30-65, Medellín 050026, Colombia
[c] TERMOMEC Research Group, Faculty of Engineering, Universidad Cooperativa de Colombia UCC, Medellín 050012, Colombia

ARTICLE INFO

Keywords:
Desmodesmus armatus
Microalga
Structured model
Tolerance mechanisms
Adsorption
Efflux

ABSTRACT

Anthropogenic activities such as mining and the metallurgical industry are the main sources of mercury contamination. Mercury is one of the most serious environmental problems in the world. This study aimed to investigate, using experimental kinetic data, the effect of different inorganic mercury (Hg^{2+}) concentrations on the response of microalga *Desmodesmus armatus* stress. Cell growth, nutrients uptake and mercury ions from the extracellular medium, and oxygen production were determined. A Compartment Structured Model allowed elucidating the phenomena of transmembrane transport, including influx and efflux of nutrients, metal ions and bioadsorption of metal ions on the cell wall, which are difficult to determine experimentally. This model was able to explain two tolerance mechanisms against mercury, the first one was the adsorption of Hg^{2+}ions onto the cell wall and the second was the efflux of mercury ions. The model predicted a competition between internalization and adsorption with a maximum tolerable concentration of 5.29 mg/L of $HgCl_2$. The kinetic data and the model showed that mercury causes physiological changes in the cell, which allow the microalga to adapt to these new conditions to counteract the toxic effects. For this reason, *D. armatus* can be considered as a Hg-tolerant microalga. This tolerance capacity is associated with the activation of the efflux as a detoxification mechanism that facilitates the maintenance of the osmotic balance for all the modeled chemical species. Furthermore, the accumulation of mercury in the cell membrane suggests the presence of thiol groups associated with its internalization, leading to the conclusion that metabolically active tolerance mechanisms are dominant over passive ones.

1. Introduction

Mercury is one of the heavy metals that is discharged into the oceans and generates one of the most serious environmental problems in the world (Li et al., 2022). Worldwide release of Hg to the sea from rivers is estimated to be 200–5500 mg y^{-1} (Liu et al., 2021). Recent environmental studies has encouraged to elucidate the dynamics of effects of Hg in marine systems (Beauvais-Flück et al., 2018; Cossart et al., 2022). In the environment, Hg can be found in three main forms:, divalent elemental mercury (Hg^0), inorganic mercury (Hg^{2+}), and methylmercury (MeHg) (Li et al., 2022). As a result, microalgae are frequently exposed to mercury, which delays their development and reproduction due to the physiological and metabolic irregularities (Pradhan et al., 2022). This can endanger the aquatic system's dynamics. Microalgae are the primary producers (phytoplankton) in marine and freshwater ecosystems therefore they play an important role (Pradhan et al., 2022), and when exposed to low concentrations of mercury, they are also the starting point for Hg to enter into the food chain (Li et al., 2022).

Metal ions can be adsorbed on the cell walls of microalgae and enter through the cell membrane via active transport by binding to thiols groups such as cysteine (Pradhan et al., 2022). Microalgae might use several types of biological responses against metal ions toxicity, classified as energetically passive or active. The first one is bioadsorption, which can occur due to physicochemical interactions between metal ions and the ionizable groups on the cell wall surface and relies on the chemical composition of the cell wall (do Nascimento et al., 2017; Fawzy et al., 2020; Spain et al., 2021); or extracellular chelation with exoproteins and exopolysaccharides (Pradhan et al., 2022). The second

* Corresponding author.
E-mail address: catalina.quevedo@udea.edu.co (C. Quevedo-Ospina).

https://doi.org/10.1016/j.aquatox.2023.106496
Received 29 October 2022; Received in revised form 15 February 2023; Accepted 12 March 2023
Available online 19 March 2023

one is bioaccumulation, which is when the cell can produce intracellular chelating agents such as phytochelatins and polyphosphate bodies (Pradhan et al., 2022); or can expulse ions from the cytoplasm to the extracellular medium through transmembrane transporters (Ibuot et al., 2020; Tripathi and Poluri, 2021). These efflux transporters can be transmembrane proteins usually used for metal ion internalization such as CDF types (Cation diffusion facilitators), ATPases, ABC transporters, and metal transporters for Zn, or they can be multidrug efflux pumps (Blaby-Haas and Merchant, 2012). This is the result of mechanisms of tolerance occurring upon exposure to divalent heavy metals processes that can be studied in the model microalga *Desmodesmus armatus* (Pokora et al., 2014). The genre of *Desmodesmus* has been shown to exhibit phenotypic plasticity and resilience, allowing survival in harsh and variable environments (Chung et al., 2018). Microalgae have been used as an essential means to assess the potential toxicity from heavy metals as they act as bio-indicators in the aquatic ecosystem (Hussain et al., 2020). For this reason, elucidating these mechanisms allow us to understand the behavior of microalgae in aquatic environments contaminated, since knowledge of the mechanisms of toxicity is essential for proper environmental risk assessment (Barón-Sola et al., 2021). However, simultaneous analyzes from the omics sciences (Beauvais--Flück et al., 2017, 2016; Ibuot et al., 2020; León-Vaz et al., 2021; Tripathi and Poluri, 2021; Vendruscolo et al., 2019) added to kinetic studies that allow reaching important conclusions about these tolerance mechanisms may not be sufficient; due to the robustness of the experimental designs required, the time required, and the lack of data for validation in microalgae. In addition, some variables are not easily measurable or cannot be followed over time (Tramontin et al., 2018). Therefore, mathematical modeling becomes a fundamental tool for describing the mechanisms of metal tolerance because it allows predicting the behavior of intermediates in places such as the wall and membrane cell, where it is not easy to take measurements. Using for this purpose extracellular kinetic data are more easily measurable. Some complex processes have been modeled such as the capture and internalization, excretion, transport, and intracellular chelation considering the concentrations of metals in the cell surface and in the extracellular medium; under cell growth-inhibiting conditions for bacteria (Duval, 2013; Duval et al., 2015; Duval and Rotureau, 2014; Galceran et al., 2006; Hajdu et al., 2010; Présent et al., 2017; Rotureau et al., 2015). Few of these studies consider that proposed models for bacteria can be extrapolated to explain the tolerance mechanisms of microalgae under heavy metal stress (Duval, 2013; Duval et al., 2015; Duval and Rotureau, 2014; Hajdu et al., 2010; Rotureau et al., 2015). Although there are few reports that address, through a mathematical model, the influence of the heavy metals ions in microalgae (Duval et al., 2015), none of them is related to the genus *Desmodesmus*. In addition, there is no information about mathematical models explaining the effect of mercury on growth, nutrient uptake, and metabolite production. Toxic metals such as Hg^{2+} represent a threat to photosynthetic microorganisms in contaminated aquatic ecosystems (Barón-Sola et al., 2021).

To have a model that represents this type of effect, in this new study, a Compartment Structured Model is presented to analyze the growth, capture, and efflux of nutrients and mercury (Hg^{2+}); transmembrane transport for all species and bioadsorption of metal ions in the cell wall, based on experimental data obtained from the culture of *Desmodesmus armatus* grown in the presence of inorganic mercury at sublethal concentrations. This model includes 4 compartments, 15 ordinary differential equations and 49 parameters. An identifiability analysis is coupled to the optimization routine given the overparameterization of the model and the high correlations between parameters. To the best of the authors' knowledge, this is the first model of its kind reported in the literature for microalgae.

2. Materials and methods

The microalgae *Desmodesmus armatus* belonging to the Bioprocess Laboratory of the Universidad de Antioquia was used and cultivated in a modified CHU-13 culture medium (Furuhashi et al., 2013). The microalgae were cultivated in 250 mL Erlenmeyer flasks. The working volume was 30 L, at a temperature of 27 °C, 140 rpm in an orbital shaker (Thermo Scientific MaxQ6000) under fluorescent light (20 μmol m^{-2} s^{-1}), and a photoperiod of 12:12 light/darkness.

The treatment solutions were supplemented or not (controls) with 5.0 mg/L de $HgCl_2$ as the threshold concentration (Capolino et al., 1997). This experimental design ensured that the initial biomass concentration was 66.5 and 100 mg/L g L^{-1}. The biomass was exposed to Hg^{2+} and the growth kinetics of *D. armatus* were studied at 0, 24, 48, 72, 96, 120, 144, 168, and 192 h. These conditions were used for the calibration and validation of the mathematical model for estimating all necessary parameters under the presence of Hg^{2+}. In addition, the growth kinetics of *D. armatus* was examined at an initial biomass concentration of 75.2 mg/L y 145.9 mg/L without Hg. The following parameters on culture media during growth kinetics were characterized: biomass production, total mercury, nitrite nitrogen (NO_2^-- N), inorganic phosphate (PO_4^{3-}- P), and dissolved oxygen (DO). All experiments were performed in triplicate.

Biomass concentration was measured using the direct dry weight method (Umetani et al., 2021; Vendruscolo et al., 2019). Total mercury was quantified by the cold vapor atomic absorption method (SM 3112-B) (Baird Roger and Laura Bridgewater, 2017). Bicarbonate was determined using alkalinity measurements through potentiometric titrations with 0.02 N H_2SO_4 (Merck) in an automatic titrator (TitronLine7000). Dissolved oxygen concentration was quantified using an oximeter (SI Analytics Lab 745). Nitrate concentration was quantified using the salicylic acid method (Palomino et al., 1997) at a wavelength of 410 nm. The phosphate concentration was determined by the ascorbic acid method (SM 4500-P E) at a wavelength of 880 nm (Baird Roger and Laura Bridgewater, 2017). All measurements are reported in mg/L.

Table 1
Outputs variables (Y).

Symbol	Description	Units
x	Biomass concentration	mg/L
C_{ext}	Extracellular bicarbonate concentration	mg/L
N_{ext}	Extracellular nitrates concentration	mg/L
P_{ext}	Extracellular phosphates concentration	mg/L
Hg_{ext}	Extracellular mercury concentration	mg/L
O	Dissolved oxygen concentration	mg/L

3. Model development

3.1. Compartment structured model for D. armatus in presence of Hg

The Compartment Structured Model proposed in this work is described as a "first principles-based model" derived from material balances for each of the species involved in the process as presented in equations Eqs. (1)–(3) (Villegas et al., 2017):

Table 2
State variables (X).

Symbol	Description	Initial condition	Units
Hg_{wall}	Mercury concentration in the cell wall	0.0	mg/g
C_{mem}	Carbon concentration in the membrane	0.1	mg/g
N_{mem}	Nitrates concentration in the membrane	0.1	mg/g
P_{mem}	Phosphates concentration in the membrane	0.1	mg/g
Hg_{mem}	Mercury concentration in the membrane	0.01	mg/g
C_{cyt}	Carbon concentration in the cytoplasm	0.01	mg/g
N_{cyt}	Nitrates concentration of in the cytoplasm	0.01	mg/g
P_{cyt}	Phosphates concentration in the cytoplasm	0.01	mg/g
Hg_{cyt}	Mercury concentration in the cytoplasm	0.0	mg/g

Table 3
Parameters.

Nomenclature			
μ_{max}	maximum growth rate (day^{-1})	$v_{max_{m2,n}}$	Maximum rate reaction nitrates to site *2* (mg N g^{-1} day^{-}
e_p	Absorption coeficient for *D. armatus* (mg X^{-1} μm^{-1} L)	$k_{m2,n}$	Nitrates to sites *2* affinity constant (mg N g^{-1})
$k_{C,ext}$	Saturation constant for carbonate (mg C L^{-1})	$v_{max_{m1,p}}$	Maximum rate reaction phosphates to sites *1* (mg P g^{-1} day^{-1})
$y_{x/c}$	Carbonate to biomass yield (mg X mg C^{-1})	$k_{m1,p}$	Phosphates to sites *1* affinity constant (mg P g^{-1})
$k_{N,ext}$	Saturation constant for nitrates (mg N L^{-1})	$v_{max_{m2,p}}$	Maximum rate reaction phosphates to site *2* (mg P g^{-1} day^{-1})
$y_{x/N}$	Nitrates to biomass yield (mg X mg N^{-1})	$k_{m2,p}$	Phosphates to sites *2* affinity constant (mg P g^{-1})
$k_{P,ext}$	Saturation constant for phosphates (mg P L^{-1})	$v_{max_{m1,Hg}}$	Maximum rate reaction mercury to sites *1* (mg Hg g^{-1} day^{-1})
$y_{x/P}$	Phosphates to biomass yield (mg X mg P^{-1})	$k_{m1,Hg}$	Mercury to sites *1* affinity constant (mg Hg g^{-1})
k_I	Saturation constant for luminous intensity (µmol m^{-2} s^{-1})	$v_{max_{m2,Hg}}$	Maximum rate reaction mercury to site *2* (mg Hg g^{-1} day^{-1})
$k_{Hg,ext}$	Biomass to mercury affinity constant (mg Hg L^{-1})	$k_{m2,Hg}$	Mercury to sites *2* affinity constant (mg Hg g^{-1})
$k_{Inh,Hg}$	Biomass inhibition constant for mercury (mg Hg L^{-1})	$k_{inf,c}$	Influx constant for carbonate (day^{-1})
k_{LaO}	Oxygen mass transfer coefficient (day^{-1})	$k_{eff,c}$	Efflux constant for carbonate (day^{-1})
O_{sat}	Oxygen saturation concentration (mg O L^{-1})	$k_{inf,n}$	Influx constant for nitrates (day^{-1})
$y_{x/O}$	Biomass to oxygen yield (mg X mg O^{-1})	$k_{eff,n}$	Efflux constant for nitrates (day^{-1})
$v_{max,cw}$	Maximum adsorption rate in cell wall (mg Hg g^{-1} day^{-1})	$k_{inf,p}$	Influx constant for phosphates (day^{-1})
k_{cw}	Cell wall to mercury affinity constant (mg Hg g^{-1})	$k_{eff,p}$	Efflux constant for phosphates (day^{-1})
$v_{max,rev}$	Maximum desorption rate from cell wall (mg Hg g^{-1} day^{-1})	$k_{inf,Hg}$	Influx constant for mercury (day^{-1})
k_{rev}	Cell wall desorption constant (mg Hg g^{-1})	$k_{eff,Hg}$	Efflux constant for mercury (day^{-1})
$v_{max_{m1,c}}$	Maximum rate reaction bicarbonate to sites *1* (mg C g^{-1} day^{-1})	$k_{C,cyt}$	Reaction constant for intracellular carbonates (day^{-1})
$k_{m1,c}$	Bicarbonate to sites *1* affinity constant (mg C g^{-1})	$k_{N,cyt}$	Reaction constant for intracellular nitrates (day^{-1})
$v_{max_{m2,c}}$	Maximum rate reaction bicarbonate to site *2* (mg C g^{-1} day^{-1})	$k_{P,cyt}$	Reaction constant for intracellular phosphates (day^{-1})
$k_{m2,c}$	Bicarbonate to sites *2* affinity constant (mg C g^{-1})	$k_{Hg,cyt}$	Reaction constant for intracellular mercury (day^{-1})
$v_{max_{m1,n}}$	Maximum rate reaction nitrates to sites *1* (mg N g^{-1} day^{-1})	v_{max,CO_2}	Maximum rate reaction bicarbonate to CO_2 (mg C L^{-1} day^{-1})
$k_{m1,n}$	Nitrates to sites *1* affinity constant (mg N g^{-1})	k_{CO_2}	Bicarbonate to CO_2 reaction constant (mg C L^{-1})
		$\mu_{CO_3^{2-}}$	Maximum rate reaction bicarbonate to CO_3^{2-} (mg C L^{-1} day^{-1})

$$\frac{dX}{dt} = f(X,t,\theta) \tag{1}$$

$$X(t_0) = X_0 \tag{2}$$

$$Y = g(X,t,\theta) \tag{3}$$

where $X = [x_1, x_2, \ldots, x_r]$ indicates the vector of state variables, t is time, $\theta = [\theta_1, \theta_2, \ldots, \theta_m]$ is the vector of model parameters, X_0 is the vector of initial conditions, and $Y = [y_1, y_2, \ldots, y_r]$ corresponds to the vector of model outputs with $n \leq r$. The nomenclature used for the model outputs and the state variables is presented in Tables 1 and 2. The model parameters can be seen in Table 3.

A Compartment Structured Model (CSM) is defined for this work as shown in Fig. 1. This model has four compartments for a single cell of *Desmodesmus armatus* under Hg^{2+} exposure: (1) extracellular compartment, (2) cell wall, (3) cell membrane, and (4) cytoplasm. Moreover, two tolerance mechanisms are included: (a) efflux that occurs at the cell membrane for metal ions and nutrients ions (Tripathi and Poluri, 2021), and, (b) bioadsorption that occurs at the cell surface (do Nascimento et al., 2017; Fawzy et al., 2020; Spain et al., 2021). Microalgae have high biosorption capacities for metals due to cell wall composition conferring the ability to bind metals via functional groups (do Nascimento et al., 2017; Fawzy et al., 2020; Spain et al., 2021). Probably the mechanism of biosorption of *Desmodesmus* occurs on the cell surface on the $Site_{CW}$ and depends on the compositions of the cell wall, the interactions between the ionizable surface groups, and the Hg^{2+} ion concentration (do Nascimento et al., 2017). Ions that do not attach to the cell wall can reach the cytoplasm through the $Site_{Hg\_m1}$ y $Site_{Hg\_m2}$. These sites are in the cell membrane and allow the transport of metal ions from the extracellular medium into the cytoplasm using a mechanism known as internalization (Duval et al., 2015; Duval and Rotureau, 2014; Hajdu et al., 2010). Internalization depends on the availability of Hg^{2+} ion-bound transmembrane proteins (Beauvais-Flück et al., 2017); thus, mercury being a non-essential metal, the microalgae must employ essential metal transporters such as ZIP, ABC, or NRAMP (Beauvais-Flück et al., 2016). After internalization, an accumulation of Hg^{2+} in the cytoplasm intoxicates the microalgae, forcing the cell to employ active mechanisms such as the expulsion of Hg ions into the extracellular medium to ensure its osmotic balance and survival (Tripathi and Poluri, 2021). This excretion mechanism is referred to as efflux and can occur through internalization sites, or efflux proteins (Tripathi and Poluri, 2021) in $Site_{Hg\_m3}$. These efflux proteins can be Cation Diffusion Family (CDF), Metal Tolerance Protein (MTP), or ABC transporters, among others (Tripathi and Poluri, 2021).

Due to the negative effect of mercury on nutrient capture and transmembrane transport (Beauvais-Flück et al., 2017, 2016), internalization and efflux mechanisms for carbon, nitrogen, and phosphorus sources are included in the model. These transport mechanisms, and the transporters, used by the microalgae are diverse, and their nature depends on the type of nutrient captured and the microalgae species (Borowitzka et al., 2016). For this reason, it is assumed that the cell can simultaneously employ two different transport sites: $Site_{HCO_3^-\_m1}$ and $Site_{HCO_3^-\_m2}$ for carbon, $Site_{NO_3^-\_m1}$ and $Site_{NO_3^-\_m2}$ for nitrogen and, $Site_{PO_4^{3-}\_m1}$ and $Site_{PO_4^{3-}\_m2}$ for phosphorus.

(1) Extracellular compartment: In this compartment the dynamics of the extracellular nutrients C_{ext}, N_{ext}, P_{ext}, Hg_{ext}, O and x are modelled. The dynamics of cell growth is presented in Eq. (4). In order to describe the specific rate of cell growth μ, in Eq. (5) an extended Monod-type equation for multiple substrates is used, where the mercury concentration behaves as an inhibitor (Tijani et al., 2018). This assumption is acceptable, considering that mercury is captured or internalized by the microalgae through transmembrane transporters, in $Site_{Hg\_m1}$ and $Site_{Hg\_m2}$, (Beauvais-Flück et al., 2017; Tripathi and Poluri, 2021) and therefore can directly affect the growth of *Desmodesmus armatus*.

$$\frac{dx}{dt} = \mu x \tag{4}$$

$$\mu = \mu_{max}\left(\prod_{i=1}^{n}\left(\frac{Z_{i,ext}}{k_{i,ext} + Z_{i,ext}}\right)\right)\left(\frac{I}{k_I + I}\right)\left(\frac{Hg_{ext}}{k_{Hg,ext} + Hg_{ext} + \frac{Hg_{ext}^2}{k_{Inh,Hg}}}\right) \tag{5}$$

where, x is the biomass concentration, μ is the growth rate, μ_{max} is the maximum growth rate, $Z_{i,ext}$ represents the concentration for each nutrient in the culture medium C_{ext}, N_{ext} and P_{ext}, $k_{i,ext}$ is the saturation

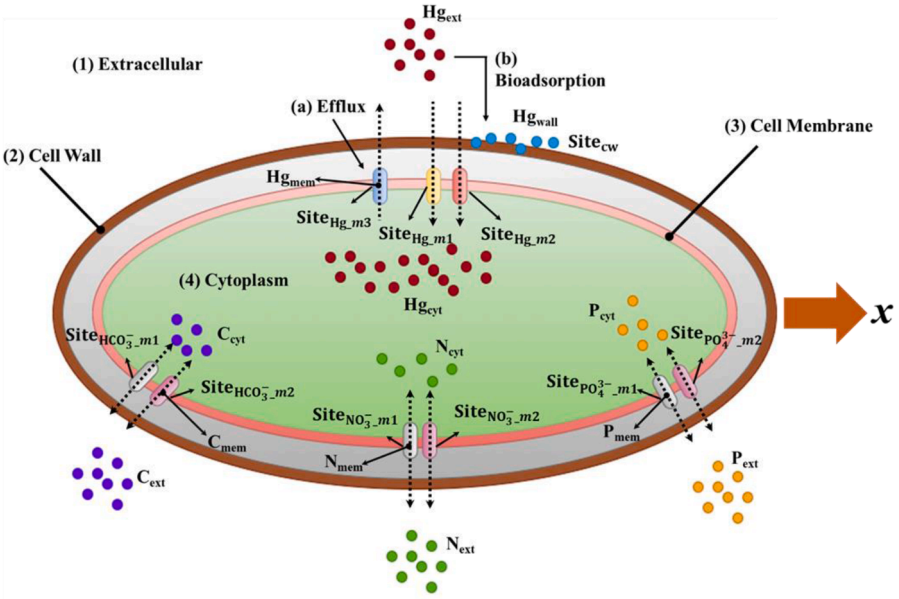

Fig. 1. Schematic representation of the Compartment Structured Model proposed for *Desmodesmus armatus* in the presence of mercury. Each subindex used corresponds to a compartment: ext (extracellular), wall (cell wall), mem (cell membrane) and cyt (cytoplasm).

constant for each nutrient, Hg_{ext} is the extracellular mercury concentration, k_I is the saturation constant for luminous intensity, $k_{Hg,ext}$ and $k_{Inh,Hg}$ are the affinity and inhibition constant for mercury. The light intensity I is considered as a substrate and is represented by Eq. (6), in an expression derived from Beer's Law (Tijani et al., 2018).

$$I = \frac{1}{e_p dx}\left(1 - I_o e^{-e_p dx}\right) \tag{6}$$

where, I_o and d are constants and were determined experimentally with values of 20 μmol m^{-2} s^{-1} and 68.6 nm, respectively. And e_p is the mean absorption coefficient. The equations that represent the dynamics for the nutrients are proposed from material balances in Eq. (7), considering the consumption rate of each nutrient, and the rate of efflux that occurs in internalization sites $Site_{HCO_3^-\_m1}$ and $Site_{HCO_3^-\_m2}$ for bicarbonate, $Site_{NO_3^-\_m1}$ and $Site_{NO_3^-\_m2}$ for nitrates, and $Site_{PO_4^{3-}\_m1}$ and $Site_{PO_4^{3-}\_m2}$ for phosphates (Beauvais-Flück et al., 2016; Hajdu et al., 2010). These proteins can be ion channels that allow passive transport by facilitated diffusion, ATPases that favor primary active transport, or ion-dependent transport proteins that are used for secondary active transport (Blaby--Haas and Merchant, 2012).

$$\frac{dZ_{i,ext}}{dt} = -\frac{\mu}{Y_{x/Z_i}} x + k_{eff,i}\, Z_{i,cyt} \tag{7}$$

where, Y_{x/Z_i} represents the biomass yield, $k_{eff,i}$ is the efflux constant and $Z_{i,cyt}$ is the cytoplasmatic concentration for each nutrient. The proposed material balance for the bicarbonate source Eq. (8) includes the consumption rate, the efflux rate, and two additional terms representing possible changes in HCO_3^- concentration caused by the shift of chemical equilibrium due to variations in pH.

$$\frac{dC_{ext}}{dt} = -\frac{\mu}{Y_{x/C}} x + k_{eff,C}\; C_{cyt} + v_{max,CO_2}\frac{C_{ext}}{k_{CO_2} + C_{ext}} - \mu_{CO_3^{2-}} e^{\mu_{CO_3^{2-}} t} \tag{8}$$

where, $Y_{x/C}$ is the carbonate to biomass yield, $k_{Z_{eff,C}}$ is the efflux constant for carbonate, C_{cyt} is the carbonate cytoplasmatic concentration, v_{max,CO_2} is the maximum rate of the reaction from bicarbonate to CO_2, k_{CO_2} is the bicarbonate to CO_2 reaction constant and $\mu_{CO_3^{2-}}$ is the maximum rate of reaction from bicarbonate to CO_3^{2-}.

The balance for extracellular mercury is shown in Eq. (9). It is governed by the rate of adsorption and the rate of desorption at the cell wall surface in $Site_{cw}$, the rate of internalization in $Site_{Hg\_m1}$ and $Site_{Hg\_m2}$, and the rate of efflux in $Site_{Hg\_m1}$, $Site_{Hg\_m2}$ and $Site_{Hg\_m3}$.

$$\frac{dHg_{ext}}{dt} = -v_{max,cw}\frac{Hg_{ext}}{k_{cw,Hg} + Hg_{ext}} + v_{max,rev}\frac{Hg_{wall}}{k_{rev,Hg} + Hg_{wall}} - v_{max_{m1,Hg}}\frac{Hg_{ext}}{k_{m1,Hg} + Hg_{ext}} + v_{max_{m2,Hg}}\frac{Hg_{ext}}{k_{m2,Hg} + Hg_{ext}} + k_{eff,Hg}\; Hg_{cyt} \tag{9}$$

where, $v_{max,cw}$ is the maximum adsorption rate on the cell wall, $k_{cw,Hg}$ is the affinity of the cell wall for mercury, $v_{max,rev}$ is the maximum desorption rate from the cell wall, $k_{rev,Hg}$ is the cell wall desorption constant, Hg_{wall} is the mercury concentration in the cell wall, $v_{max_{m1,Hg}}$ and $v_{max_{m2,Hg}}$ are the maximum reaction rate for mercury to sites $Site_{Hg\_m1}$ and $Site_{Hg\_m2}$, respectively. $k_{m1,Hg}$ and $k_{m2,Hg}$ are the mercury affinity constant to sites $Site_{Hg\_m1}$ and $Site_{Hg\_m2}$, respectively. $k_{eff,Hg}$ is the efflux constant for Hg and Hg_{cyt} is the cytoplasmatic concentration of Hg. Dissolved oxygen production due to metabolism, shown in Eq. (10), depends on cell growth and mass transfer of oxygen from the cells to the culture medium.

$$\frac{dO}{dt} = \frac{\mu}{Y_{x/O}} X + k_{LaO}(O_{sat} - O) \tag{10}$$

where, O is the dissolved oxygen concentration in the culture medium, $Y_{x/O}$ is the biomass to oxygen yield, k_{LaO} is the oxygen mass transfer coefficient, and O_{sat} is the oxygen saturation concentration.

(2) Cell wall compartment: The Hg_{cw} dynamic in Eq. (11), is described from a mass balance that includes mercury adsorption and desorption as interaction mechanisms between metal ions and the cell wall. This process is metabolically passive (do Nascimento et al., 2017).

$$\frac{dHg_{wall}}{dt} = v_{max,cw}\frac{Hg_{ext}}{k_{cw,Hg} + Hg_{ext}} - v_{max,rev}\frac{Hg_{wall}}{k_{rev,Hg} + Hg_{wall}} \tag{11}$$

(3) Cell membrane compartment: The C_{mem}, N_{mem}, P_{mem} and Hg_{mem} dynamics associates with the transport or internalization of nutrient ions in Eq. (12) and mercury in Eq. (13) occurs in the cell membrane through transported $Site_{HCO_3^-\_m1}$ and $Site_{HCO_3^-\_m2}$ for bicarbonate, $Site_{NO_3^-\_m1}$ and $Site_{NO_3^-\_m2}$ for nitrates, $Site_{PO_4^{3-}\_m1}$ and $Site_{PO_4^{3-}\_m2}$ for phosphates, and $Site_{Hg\_m1}$ and $Site_{Hg\_m2}$ for mercury. The Michaelis-Menten equation is

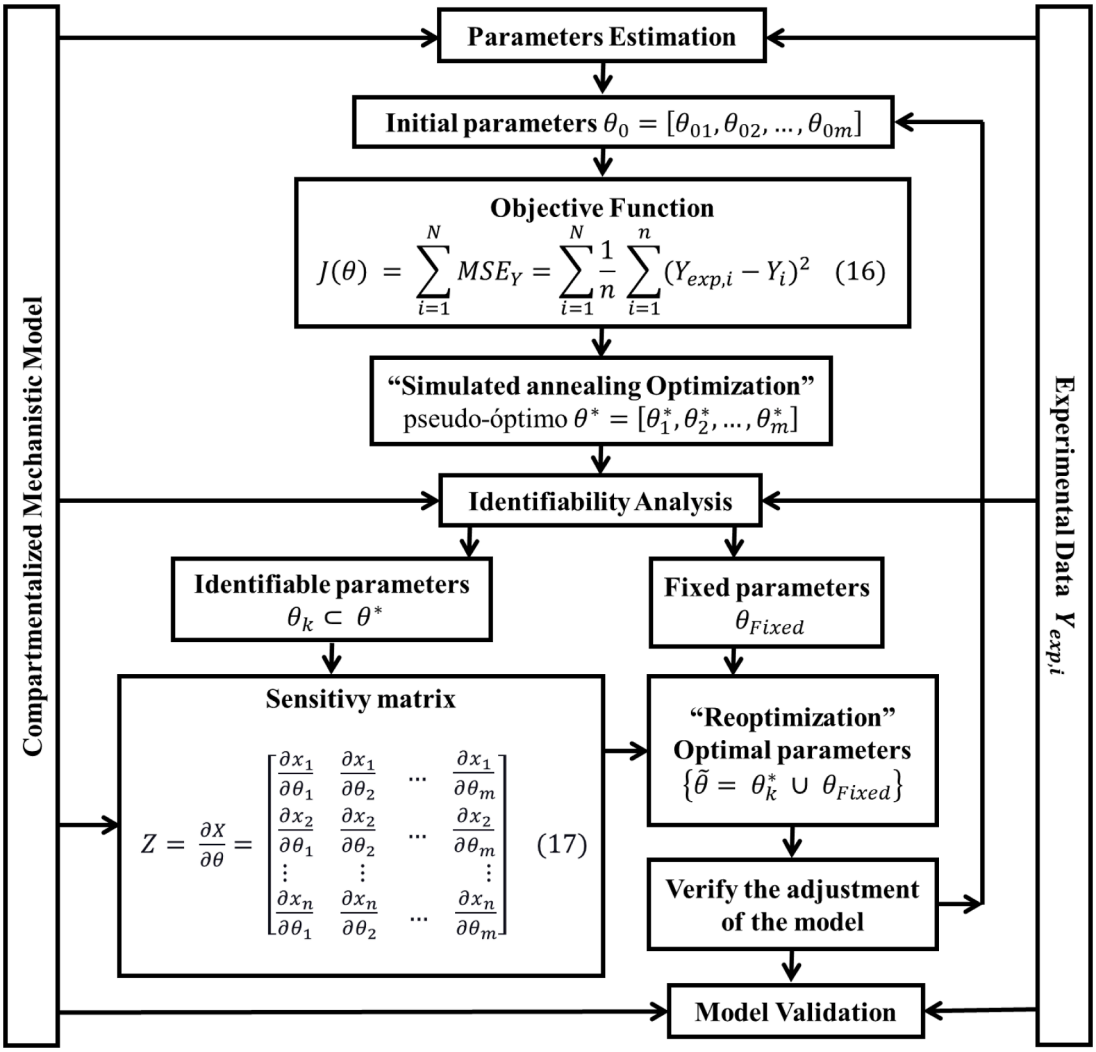

Fig. 2. Methodology for parameter estimation.

used to explain these mechanisms, assuming that transport is possible simultaneously through both sites:

$$\frac{dZ_{i,mem}}{dt} = v_{max_{m1,i}} \frac{Z_{i,ext}}{k_{m1,i} + Z_{i,ext}} + v_{max_{m2,i}} \frac{Z_{i,ext}}{k_{m2,i} + Z_{i,ext}} \quad (12)$$

$$\frac{dHg_{mem}}{dt} = v_{max_{m1,Hg}} \frac{Hg_{ext}}{k_{m1,Hg} + Hg_{ext}} + v_{max_{m2,Hg}} \frac{Hg_{ext}}{k_{m2,Hg} + Hg_{ext}} \quad (13)$$

where, $Z_{i,mem}$ is the concentration of each nutrient in the cell membrane, $v_{max_{m1,i}}$ and $v_{max_{m2,i}}$ are the maximum rate of transport for each nutrient through the sites 1 and 2, respectively. In addition, $k_{m1,i}$ and $k_{m2,i}$ are the affinity constants for each nutrient in the sites 1 and 2, respectively. Hg_{mem} is the concentration of mercury in the cell membrane, $v_{max_{m1,Hg}}$ and $v_{max_{m2,Hg}}$ are the maximum rate of transport for mercury through the sites 1 and 2, respectively. $k_{m1,Hg}$ and $k_{m2,Hg}$ are the affinity constants for mercury in the sites 1 and 2, respectively.

(4) Cytoplasm compartment: In this compartment, Eq. (14) is used to describes the cytoplasmic concentrations of the nutrients C_{cyt}, N_{cyt} and P_{cyt}, and Eq. (15) is used for mercury Hg_{cyt}. These balances include mass transfer from the cell membrane to the cytoplasm and from the cytoplasm to the extracellular medium, which are the influx and efflux rates, and the biotransformation of all species due to cellular metabolism.

$$\frac{dZ_{i,cyt}}{dt} = k_{inf,i}\ Z_{i,mem} - \ k_{eff,i}\ Z_{i,cyt} - \ k_{i,cyt} Z_{i,cyt} \quad (14)$$

$$\frac{dHg_{cyt}}{dt} = k_{inf,Hg}\ Hg_{mem} - \ k_{eff,Hg}\ Hg_{cyt} - k_{Hg,cyt} Hg_{cyt} \quad (15)$$

where, $k_{inf,i}$ and $k_{inf,Hg}$ represent the influx constants for each nutrient and mercury, respectively. In addition, $k_{i,cyt}$ and $k_{Hg,cyt}$ are the reaction constant for the intracellular nutrients and mercury.

3.2. Kinetic growth model without Hg

The kinetic parameters of the microalgae in the absence of Hg were determined using a cell kinetic growth model (KGM) derived from the CSM model. For this purpose, equations Eqs. (4)–(8) were selected. Eq. (5), Eq. (7) and Eq. (8) were modified such that the effects of mercury and nutrient efflux were not considered. KGM calibration was based on experimental measurements in absence of the Hg. This model resulted in 5 ordinary differential equations and 12 parameters. The details of the model KGM can be consulted in the supplemental material (Appendix A).

4. Estimation of parameters of CSM and KGM

The methodology describes in Fig. 2 was used in the estimation of parameters. For this, the objective function was given by *Eq.* (16), using the least squares method, where $Y_{exp,i}$ corresponds to the experimental data points and Y_i represented the predictions of the model. The initial

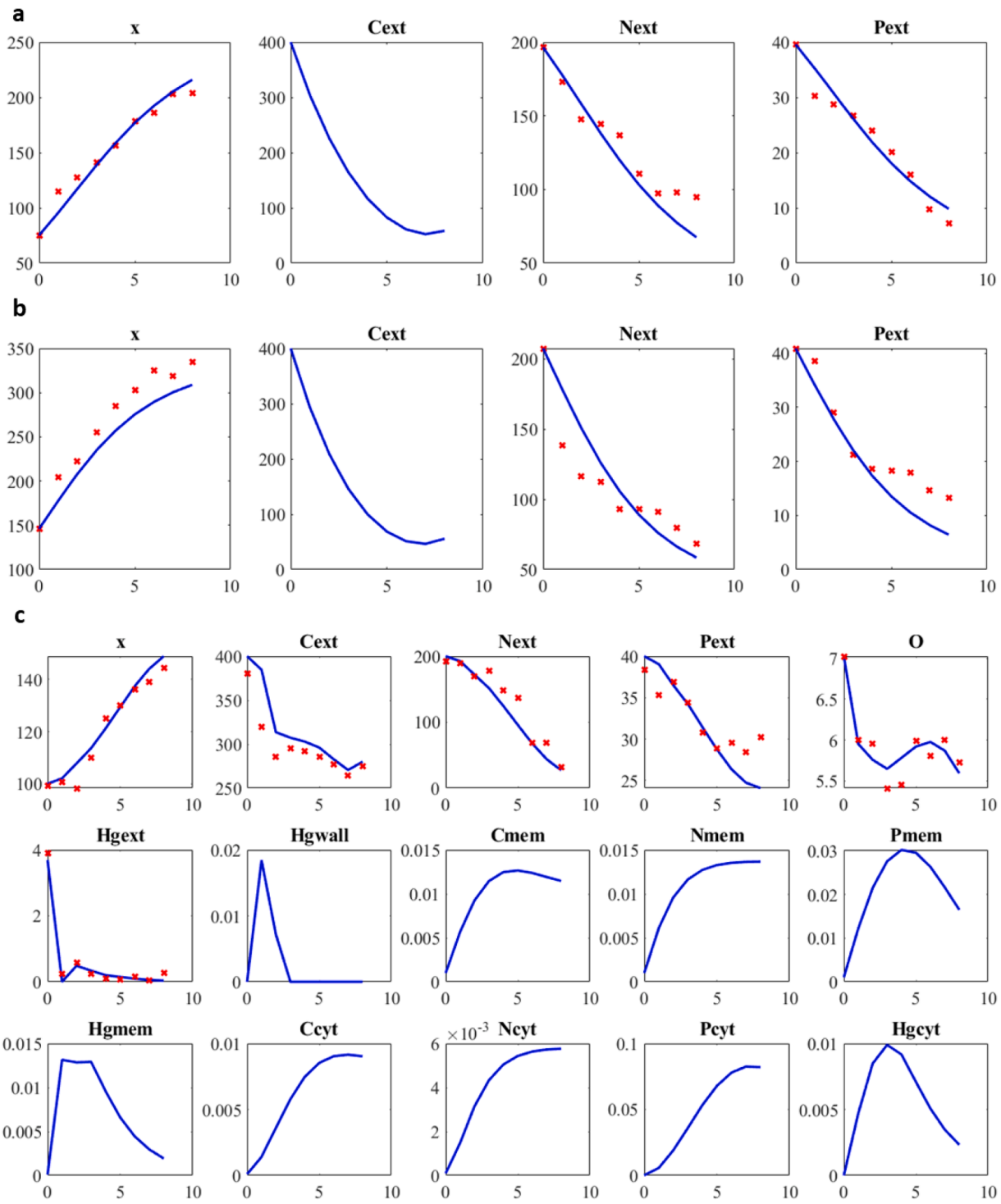

Fig. 3. Experimental data (*) and parameter estimation (–) at initial biomass concentrations of (a) **75.2 mg/L y (b) 145.9 mg/L without mercury** and (c) at initial biomass and mercury concentrations of 100 mg/L and 5.0 mg/L, respectively.

parameters θ_0 to CSM were accordingly with experimental conditions, while initial parameters to KGM were uptake from the final parameters of CSM $\widetilde{\theta}$. The "Simulated Annealing" optimization algorithm was used to determine the pseudo-optimal parameters θ^* from which the parameter identifiability process is carried out. This allows solving the difficulties associated with the overparameterization of the model, its non-linear nature and the strong correlation between the effects of the parameters, following the methodology proposed by Villegas et al. (2017). For this analysis, the θ^* parameters were divided into two subgroups: the identifiable parameters θ_k that have high effects on the objective function and low linear dependence, and the θ_{Fixed} parameters that are fixed at their initial values. Subsequently, the sensitivity matrix shown in *Eq.* (17) was used to determine any exact linear relationship between the parameters. This matrix was constructed by deriving the state variables x_i with respect to the identifiable parameters, according to the orthogonal method proposed by Yao et al. (2003). Applying a new optimization routine, the identifiable parameters θ_k^* was established, and those was used to build the group of optimal parameters $\widetilde{\theta}$, which

Table 4
Initial and optimal parameters in the proposed model.

Number	Symbol	value subset θ_0	value Final set $\widetilde{\theta}$ With Hg	Without Hg
1	μ_{max}	0.4514	0.3508	1.0092
2	e_p	0.0234	7.9927×10^{-5}	0.5207
3	k_C	0.7197	1.2126×10^{-3}	0.1741
4	$y_{x/c}$	0.6495	2.6604×10^{-2}	0.9493
5	k_N	56.6700	48.8880	99.9816
6	$y_{x/N}$	0.3003	0.2772	1.0931
7	k_P	64.8600	53.8900	39.0566
8	$y_{x/P}$	4.5640	2.0660	4.7309
9	k_I	1.1050	6.6450	1.1113×10^{-4}
10	k_{Hg}	0.3770	0.1483	
11	k_{Inh}	0.7711	0.2491	
12	k_{LaO}	0.5629	0.5677	
13	O_{sat}	1.6810	3.9850	
14	$y_{x/O}$	36.4300	67.8600	
15	$v_{max,cw}$	0.3631	0.4231	
16	k_{cw}	0.2464	0.1902	
17	$v_{max,rev}$	0.5991	0.8960	
18	k_{rev}	0.5380	0.3564	
19	$v_{max,m1c}$	0.9996	0.5069	
20	k_{m1c}	0.0036738	0.4393	
21	$v_{max,m2c}$	0.9997	1.5099×10^{-4}	
22	k_{m2c}	0.0029916	0.1138	
23	$v_{max,m1n}$	0.3002	5.7499×10^{-2}	
24	k_{m1n}	0.8242	0.6911	
25	$v_{max,m2n}$	0.1708	0.5252	
26	k_{m2n}	0.7751	0.2407	
27	$v_{max,m1p}$	0.2156	0.2157	
28	k_{m1p}	0.5255	0.5255	
29	$v_{max,m2p}$	0.5761	0.9737	
30	k_{m2p}	0.8242	0.8242	
31	$v_{max,m1Hg}$	0.2494	0.8832	
32	k_{m1Hg}	0.1633	0.5486	
33	$v_{max,m2Hg}$	0.7486	0.9992	
34	k_{m2Hg}	0.8034	0.4671	
35	k_{infc}	0.9994	0.5077	
36	k_{effc}	0.9655	0.6067	
37	k_{infn}	0.00187	0.6738	
38	k_{effn}	0.2115	1.0000	
39	k_{infp}	0.3792	0.9273	
40	k_{effp}	0.1414	0.2013	
41	k_{infHg}	0.2986	0.9402	
42	k_{effHg}	0.2427	1.0000	
43	k_{Z_C}	0.0117	5.7024×10^{-2}	
44	k_{Z_N}	0.3810	0.5943	
45	k_{Z_P}	0.1136	1.7301×10^{-2}	
46	$k_{Z_{Hg}}$	0.5215	0.1645	
47	v_{max,CO_2}	0.9842	0.9842	0.7540
48	k_{CO_2}	0.2163	0.2155	0.5461
49	$\mu_{CO_3^{2-}}$	0.5400	0.8070	0.5306

was reoptimized to verify the fit of the model. If these parameters were acceptable, the model was then validated with experimental data, otherwise, these parameters will be used to start the process again, that is, $\theta_0 = \widetilde{\theta}$. The details of the identifiability analysis can be consulted in the supplemental material (Appendix B). In the following section, the results of the optimal parameters of the model are presented. All scripts needed to mathematically solve the model were developed in matlab R2020b software licensed for academic use by Universidad de Antioquia UdeA and Universidad Cooperativa de Colombia UCC.

From the data obtained for the maximum cell growth rates in the CSM and KGM models, the doubling time t_d was calculated using the following expression:

$$t_d = \frac{Ln2}{\mu_{max}} \tag{18}$$

5. Results and discussion

5.1. Parameters fitting and validation

Fig. 3a and 3b show the experimental data and the results of the optimal kinetic parameter fit for KGM. The kinetics at both initial biomass concentrations present a good fit for biomass x, extracellular nitrogen N_{ext} and phosphorus P_{ext}. Fig. 3c show the experimental kinetic data and the results of the parameters fitting using the optimal parameters $\widetilde{\theta}$ for CSM. The model presented a good fit for biomass x, extracellular carbon C_{ext}, nitrogen N_{ext} and phosphorus P_{ext}, oxygen O, and total extracellular mercury Hg_{ext}. The minimum square error MSE_Y found for this data set was 0.0445 and 0.1219, respectively.

Table 4 show the values for initial and optimal parameters to models CSM y KGM. *D. armatus* physiology responses to Hg exposure were determined. All parameters, including maximum growth velocity (μ_{max}), cell division (t_d), ability to absorb light (e_p) and dry biomass concentration (Fig. 3c), were altered in microalga.

The maximum growth velocity was 2.88-fold higher in control (without Hg) than in microalgae under Hg treatment. In *D. armatus*, the cell division was 1.98 day with Hg compared to the cell division of 0.69 day without Hg. The inhibition of growth and shorter life cycles have been associated with microalgae cells under exposure to low concentrations of Hg (Ge et al., 2022). These variations cause changes in the biomass production of *D. armatus* on the first two days of the kinetics of growth, where the production biomass level was lowest at 1.24% with respect to the initial concentration obtained (Fig. 3c). Possibly, the inhibitory effects on the *D. armatus* in the early days of kinetics are due to deterioration in the activity of antioxidant enzymes, which leads to an increase in the concentrations of reactive oxygen species (Capolino et al., 1997; Ge et al., 2022). Also, the ability to absorb light of the cell of *D. armatus* grown in Hg was significantly lower (6515-fouls) than controls. e_p under cells without Hg exposure, indicating that the light absorption photosystem PSII had a sensitivity towards high Hg^{2+} concentrations on the first days of growth (Ge et al., 2022). Therefore, it decreased its efficiency in the photosynthesis process due to the instability of chlorophyll to do out their energy interconversions by chemiosmotic mechanisms under abiotic stress (Ge et al., 2022).

The model CSM validation shows tendencies of model and experimental data for biomass, nitrogen, and phosphorus (Fig. 4). The results show that the model has a good predictive capacity. The minimum square error MSE_Y found for this data set was 0.3983.

5.2. Adsorption on the cell wall

The model, through the variable Hg_{cw}, predicts a rapid adsorption of mercury in the cell wall and a complete and slower desorption that ends on day three. Simultaneously mercury ions are internalized Hg_{mem}, and this capture of ions is dominant after day three when it is no longer possible to find mercury in the wall as shown in Fig. 3. The results indicate that the cell wall of the *D. armatus* has ionizable groups that interact and binding with Hg^{2+} ions as mechanisms of absorption (do Nascimento et al., 2017; Spain et al., 2021). The absence of mercury in the cell wall has been previously reported by do Nascimento et al. for *Chlamydomonas reinhardtii* (do Nascimento et al., 2017), who attributed this behavior to the fact that part of the mercury was internalized, and the mercury adsorbed on the cell wall can only occupy a fraction of the available binding sites. These observations allow us to infer that the interactions of mercury with the ionizable wall groups of *D. armatus* are not strong enough for this mechanism to be dominant in live cultures, because neutral mercury species such as $HgCl_2$ can be more easily transported through the cell membrane than other species (Beauvais--Flück et al., 2018). In addition, it is possible that the metabolically active mechanisms, subsequent to the internalization of mercury, may be more relevant for the survival of the microalga than the passive mechanisms

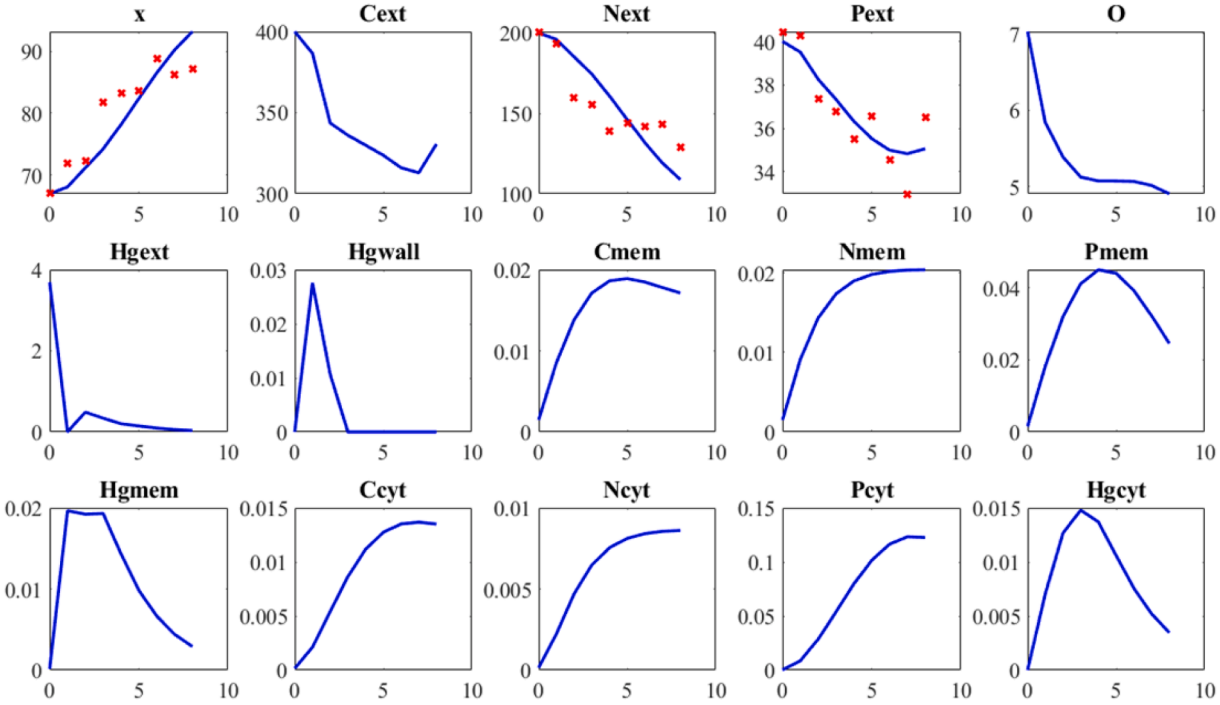

Fig. 4. Model validation (–) using experimental data (*) for biomass, and extracellular nitrogen and phosphorus, at initial biomass and mercury concentrations of 66.95 mg/L and 5.0 mg/L, respectively.

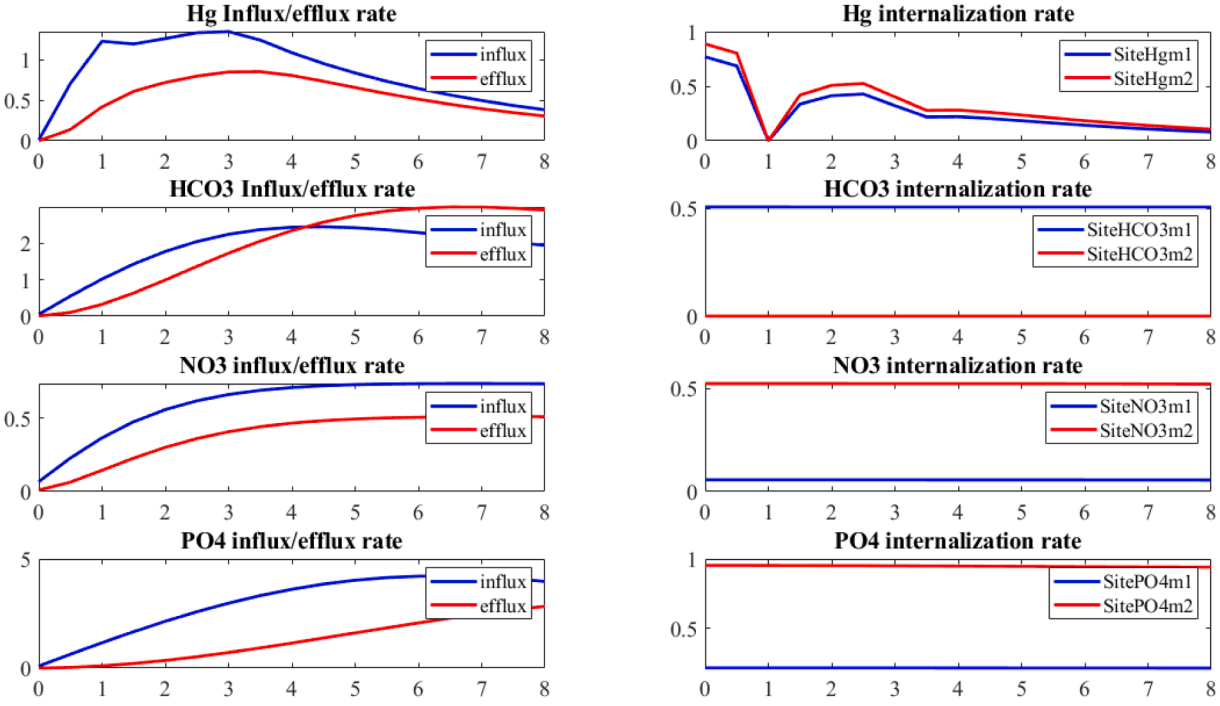

Fig. 5. Model predictions for influx/efflux phenomena and transmembrane transport rates across transporters sites. The x-axis corresponds to the culture time expressed in days, while the y-axis corresponds to the influx/efflux rates and transport rates expressed in mg of each species g^{-1} day^{-1}.

such as adsorption, or it is also possible that the interactions with the cell wall constitute the first step for the mechanism of bioaccumulation (Tripathi and Poluri, 2021).

5.3. Transmembrane transport and efflux

The model showed the phenomena associated with the transmembrane transport of nutrients and mercury, both the influx and efflux rates (Fig. 5). To properly validate Compartment Structured Model phenomena associated with the transmembrane internalization were assumed two transporters to mercury, carbon, nitrogen, and phosphorus.

The model shows that the influx and efflux rates for all nutrients tend to reach a steady state after day 3. In addition, the efflux rate for

nitrogen and phosphorus is lower than the influx rate, while for carbon the rate of efflux is slightly greater at the end of the kinetics. A higher rate of efflux for inorganic carbon may be associated with a reduction in the energetic metabolism due to the negative influence of mercury on it, causing a greater accumulation of carbon inside the cell and, therefore, its expulsion from the cytoplasm to a higher rate (Beauvais-Flück et al., 2017). A similar behavior was observed for Barón-Sola et al. (2021) in the microalga *Chlamydomonas acidophila,* where the microalga reflects alterations in carbon metabolism in response to Cd and Hg stress.

For mercury, it is observed that the influx is greater until day five, and thereafter, the rates of influx and efflux are similar. These results are consistent with the osmotic balance between the extracellular medium and the cytoplasm, suggesting that the efflux mechanism used by the microalgae is effective in guaranteeing their survival (Blaby-Haas and Merchant, 2012). This resistance mechanism has been widely described in bacteria capable of using it as a first line of defense through efflux pump-type proteins to counteract the effect of different types of antibiotics (Priyadarshanee et al., 2022). These transporters can be used against toxic heavy metals such as mercury by the action of resistance genes such as the *mer* operon that confer antibiotic and heavy metal

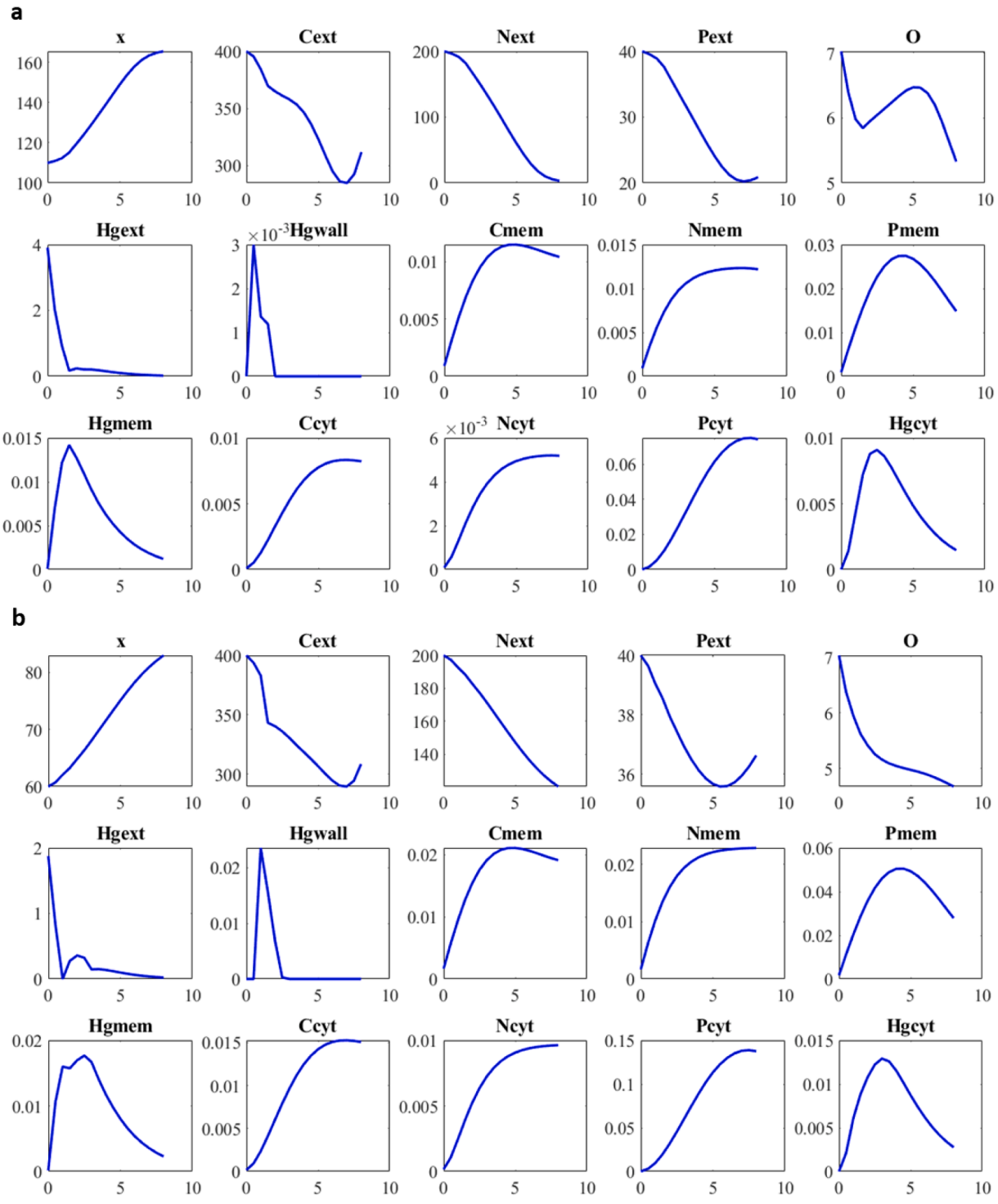

Fig. 6. Simulations at different initial culture conditions. (a) 110 mg/L biomass and 5.29 mg/L $HgCl_2$. (b) 60 mg/L biomass and 2.54 mg/L $HgCl_2$.

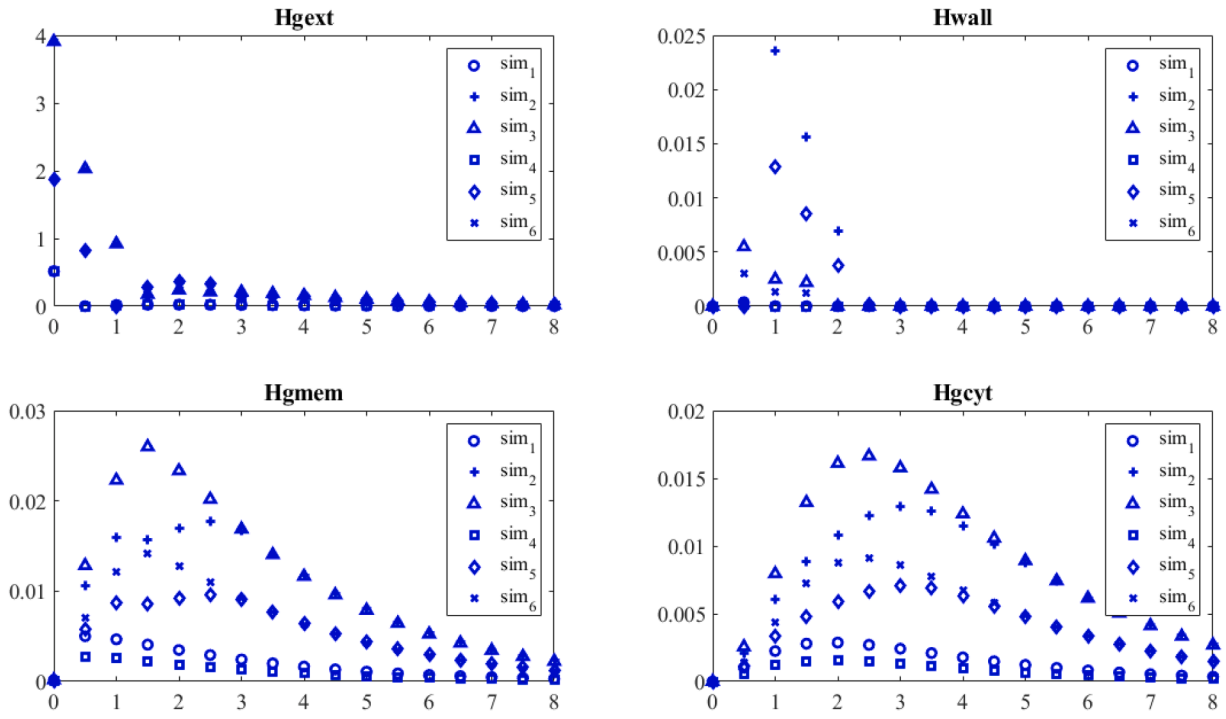

Fig. 7. Simulations of Hg compartmentalization at different initial conditions. Sim_1 at 60 mg/L biomass and 0.7 mg/L $HgCl_2$, Sim_2 at 60 mg/L biomass and 2.54 mg/L $HgCl_2$, Sim_3 at 60 mg/L biomass and 5.29 mg/L $HgCl_2$, Sim_4 at 110 mg/L biomass and 0.7 mg/L $HgCl_2$, Sim_5 at 110 mg/L biomass and 2.54 mg/L $HgCl_2$ and Sim_6 at 110 mg/L biomass and 5.29 mg/L $HgCl_2$.

resistance (Priyadarshanee et al., 2022). In turn, this mechanism can be found in other organisms such as plants that can use metal transporters classified into several families, such as ZIP, NRAMPs and MTPs (Yan et al., 2020) for influx/efflux of metal ions and other toxic substances. Algae, like plants, can allow efflux through transporters typically used for ion capture under metal stress conditions or employ heavy metal ATPases (HMA), Cation Efflux Proteins (CE) or cation diffusion family (CDF) which are also called metal tolerance proteins (MTP) (Beauvais-Flück et al., 2017, 2016; Ibuot et al., 2020; Tripathi and Poluri, 2021).

The rate of transport through the sites $Site_{HCO_3^-\_m1}$, $Site_{HCO_3^-\_m2}$, $Site_{NO_3^-\_m1}$, $Site_{NO_3^-\_m2}$, $Site_{PO_4^{3-}\_m1}$, and $Site_{PO_4^{3-}\_m2}$ in remain constant. The $Site_{HCO_3^-\_m2}$ y $Site_{PO_4^{3-}\_m1}$ showed zero rate suggesting that the nitrogen and phosphorus may have been internalized by one transporter. On the other hand, the rates $Site_{Hg\_m1}$ and $Site_{Hg\_m2}$ in D. armatus may indicate that the transport of mercury across the transmembrane proteins is not a continuous process, as well the carrying of the divalent mercury probably does different membrane proteins in the microalgae, transport mechanism across the cell membrane has been associated with binding to either ion carriers or low molecular weight thiols, allowing metals to penetrate as mercury (Balzano et al., 2020; Pradhan et al., 2022).

These transmembrane transporters for mercury may be the same ZIP and ABC used for the transport of essential metal ions, since the genes that regulate these proteins may be upregulated by the presence of inorganic mercury and methylmercury, as reported by Beauvais et al. (Beauvais-Flück et al., 2016). This phenomenon can also be found in plants, where ZIP transporters are used to capture divalent ions such as Fe^{2+}, Mn^{2+} y Cd^{2+} (Yan et al., 2020), which share the valence of the Hg^{2+} ion present in mercuric chloride.

5.4. Nutrients and metabolism

Nutrient consumption of nitrogen, phosphorus, and carbon exhibit significant differences between *D. armatus* cells exposure to Hg and control cells without mercury (Table 4). Mercury exposure reduced the nitrogen consumption in *D. armatus* after 48 h was 2.81 - 3.37-fold least in cell contact with Hg than cell control (75.2 mg/L initial inoculums and 145.9 mg/L initial inoculum, respectively). After 24 h and 48 h Hg exposure, the cell P consumption was reduced in *D. armatus* (Table 4). Under control conditions, *D. armatus* cells were 2.48-fold (75.2 mg/L initial inoculums) and 3.21-fold (145.9 mg/L initial inoculum) have higher P concentrations than those of cells with Hg. Mercury exposure resulted in a more significant reduction of the consumption of carbon in *D. armatus* than in the control cell (2.23 and 2.41-fold higher than in cells under Hg). This behavior is consistent with what was found by Beauvais-Flück et al. (2017, 2016) who report alterations in enzymatic mechanisms such as CCMs (CO_2 concentrating mechanisms) which are that allow the extracellular transformation of bicarbonate into CO_2 and is linked to primary metabolism, energy reserves, biomass production and the thermodynamic equilibrium of microalgae (Beauvais-Flück et al., 2016). This could have harmed the biomass concentration since the Hg can be altering the energy metabolism and carbon acquisition (Beauvais-Flück et al., 2017). Hence, microalgae must thus change their way of adapting to survive in such an environment activating a mechanism to respond to stress conditions (Pradhan et al., 2022). In this study, microalga could recover the consumption of the nutrients at 72 h the Hg-exposure. As in some plants, pattern response to abiotic stress consists of an ion interacting with the cell, possibly involving may specific receptor on the membrane plasma to induce the expression of the mechanism's tolerance (Ma et al., 2001).

On the other hand, León-Vaz et al. (2021), through a proteomic analysis in *Chlorella sorokiniana* contaminated with cadmium, found alterations in the regulation of enzymes associated with the synthesis of amino acids such as cysteine, methionine, glycine and glutamate, necessary for the synthesis of free thiol groups such as glutathione (Piotrowska-Niczyporuk et al., 2017), and phytochelatins (Piotrowska-Niczyporuk et al., 2017; Pradhan et al., 2022), which allows us to infer that the presence of heavy metals induces the detouring of metabolism to the production of these chelating agents as detoxification

mechanisms to the detriment of energy metabolism and biomass production. In *Chlamydomonas reinhardtii* under different times and doses of mercury, the microalga present metabolic alterations in carbohydrates, proteins, and lipids. In addition, mercury triggers intracellular oxidative stress and chloroplast damage (Barón-Sola et al., 2021).

From the metabolic point of view and under the proposed stress conditions, oxygen is a metabolite of great importance and the effects of mercury on its production account for the toxic effects suffered by the microalgae (Capolino et al., 1997). In this regard, it can be observed in Fig. 3 that the maximum concentration of cytoplasmic mercury Hg_{cyt} on day three coincides with the minimum concentration of dissolved oxygen *O*. This suggests that, during the first three days, the cells undergo important metabolic alterations that limit oxygen production causing its depletion (Beauvais-Flück et al., 2016). However, after these three days, a stabilization of dissolved oxygen is observed, possibly caused by the biotransformation of mercury. These findings are comparable to those reported by Capolino et al. (1997) who observed a decrease in the evolution of oxygen for two microalgae of the *Scenedesmaceae* family. Also, it has been observed that photosynthesis activity (O_2 release) is drastically reduced as metal concentration increases, and is inhibited in *Chlamydomonas* exposed to Hg, a toxic effect that may limit ATP availability, promote increased ATP demand to overcome toxicity and/or hinder phosphate metabolism (Barón-Sola et al., 2021). Ssuggesting that *Desmodesmus armatus* has an increased ability to adjust to mercury stress conditions. This important effort of *Desmodesmus armatus* to counteract the effect of mercury can be considered, which consequently produces changes that allow adapted physiological parameters to new conditions (Pradhan et al., 2022). Under these conditions and according to the experimental results and models predictions, *Desmodesmus armatus* can be classified as a mercury-tolerant microalga (Capolino et al., 1997).

5.5. Simulations

By simulating different scenarios for the initial concentrations of biomass and mercury, the conditions under which the model satisfactorily predicts the behavior of *D. armatus* in the presence of mercury are established. Fig. 6 shows two of these simulations, the first one using values of 110 mg/L biomass and 5.29 mg/L $HgCl_2$ and the second one using values of 60 mg/L biomass and 2.54 mg/L $HgCl_2$.

From these simulations (Fig. 6) it is predicted that biomass production can reach between 27% and 32%, with a carbon consumption between 22% and 29%, a phosphorus capture in a range between 14% and 47% and a consumption of nitrogen more efficiently at high concentrations of biomass with 96%, while at low concentrations only 49% is consumed. The percentage of mercury removal is greater than 98% with a range of mercury adsorption in the cell wall between 2.36×10^{-2} mg/g and 2.00×10^{-4} mg/g. In all scenarios, a complete reduction of Hg on cell wall is predicted. The behavior of Hg in the cell membrane depends on the initial biomass and mercury concentrations (Fig. 7), reaching maximum values between 2.73×10^{-3} mg/g (110 mg/L biomass and 0.7 mg/L $HgCl_2$) y 0.1418 mg/g (60 mg/L biomass and 5.29 mg/L $HgCl_2$). The cell membrane compartment presents an accumulation of Hg, possibly associated with the structure and aminoacidic composition of the transporter proteins (Beauvais-Flück et al., 2016). The Hg concentration in the cytoplasm, for all scenarios, was lower than the concentration in the membrane (Fig. 7), due to the formation of chelating complexes as an active tolerance mechanism (Cossart et al., 2022). Simultaneously, at higher concentrations of Hg in the cell membrane and cytoplasm, oxygen decays to values below 5 mg/L. This behavior is indicative of metabolic damage is less severe at low concentrations. In addition, it is confirmed that internalization is predominant over adsorption and that *Desmosdesmus armatus* is a mercury-tolerant microalga with a sublethal concentration of 5.29 mg/L $HgCl_2$, which is higher than that reported by Capolino et al. (1997) for the acclimated strain.

6. Conclusions

This work developed a new Compartment Structured Model (CSM) for the cell growth of Desmodesmus armatus in mercury's presence. The model allows for explaining the mechanisms of adsorption on the cell wall, internalization, and efflux for mercury and nutrients, using extracellular kinetic data that can be easily measured. CSM relates these tolerance mechanisms with experimental data for cell growth, mercury uptake, nutrient uptake, and oxygen release. Calibration of the model using these experimental data allows obtained kinetic parameter values that contribute to the study of the tolerance mechanisms, kinetics, and modeling of microalgae in heavy metals' presence. In addition, the CSM can predict the behavior of variables in the cell wall and cell membrane that are difficult to measure, thus improving the understanding of the mechanisms of heavy metal transport in microalgae and their effect on nutrients. As this model is a first approximation to the modeling of tolerance and detoxification mechanisms in microalgae coupled to cell growth, it is recommended to carry out a more significant number of experiments that permit improving the validation of the model and increasing its robustness involving other tolerance mechanisms.

Funding sources

This work was supported by the Ministry of Science, Technology, and Innovation of Colombia through Grant No. 727 of 2015 of National Doctorates of Minciencias. And to the Universidad Cooperativa de Colombia UCC through project No. 1879.

Statement of informed consents

There were no conflicts or need for informed consent related to human or animal rights during the development of this work.

CRediT authorship contribution statement

Catalina Quevedo-Ospina: Conceptualization, Data curation, Formal analysis, Funding acquisition, Investigation, Methodology, Project administration, Resources, Validation, Visualization, Writing – original draft, Writing – review & editing. **Catalina Arroyave:** Methodology, Supervision, Writing – review & editing. **Mariana Peñuela-Vásquez:** Funding acquisition, Methodology, Project administration, Resources, Supervision, Writing – review & editing. **Adriana Villegas:** Funding acquisition, Methodology, Project administration, Software, Supervision, Writing – review & editing.

Declaration of Competing Interest

All authors declare that they have no financial or personal interests that could have any influence on the work carried out in this research and reported in this article.

Data availability

Data will be made available on request.

Appendix A. Growth kinetic model for *Desmodesmus armatus* without mercury

The growth of *Desmodesmus armatus* under normal culture conditions is present in Eq. (A.1). The growth rate was expressed using a Multiple

substrate Monod's Equations Eq. (A.2).

$$\frac{dx}{dt} = \mu x \tag{A.1}$$

$$\mu = \mu_{max}\left(\prod_{i=1}^{n}\left(\frac{Z_{i,ext}}{k_{i,ext} + Z_{i,ext}}\right)\right)\left(\frac{I}{k_I + I}\right) \tag{A.2}$$

where, x is the biomass concentration, μ is the growth rate, μ_{max} is the maximum growth rate, $Z_{i,ext}$ represents the concentration for each nutrient in the culture medium C_{ext}, N_{ext} and P_{ext}, $k_{i,ext}$ is the saturation constant for each nutrient, k_I is the saturation constant for luminous intensity. The light intensity I is considered as a substrate and is represented by Eq. (A.3), in an expression derived from Beer's Law (Tijani et al., 2018).

$$I = \frac{1}{e_p dx}\left(1 - I_o e^{-e_p dx}\right) \tag{A.3}$$

where, I_o and d are constants and were determined experimentally with values of 20 μmol m^{-2} s^{-1} and 68.6 nm, respectively. And e_p is the mean absorption spectral coefficient.

$$\frac{dZ_{i,ext}}{dt} = -\frac{\mu}{Y_{x/Z_i}} x \tag{A.4}$$

where, Y_{x/Z_i} represents the biomass yield, $k_{eff,i}$ is the efflux constant and $Z_{i,cyt}$ is the cytoplasmatic concentration for each nutrient. The proposed material balance for the bicarbonate source $Eq.\ (A.5)$ includes the consumption rate and two additional terms representing possible changes in HCO_3^- concentration caused by the shift of chemical equilibrium due to variations in pH.

$$\frac{dC_{ext}}{dt} = -\frac{\mu}{Y_{x/C}} x + v_{max,CO_2}\frac{C_{ext}}{k_{CO_2} + C_{ext}} - \mu_{CO_3^{2-}} e^{\mu_{CO_3^{2-}} t} \tag{A.5}$$

where, $Y_{x/C}$ is the carbonate to biomass yield, v_{max,CO_2} is the maximum rate of the reaction from bicarbonate to CO_2, k_{CO_2} is the bicarbonate to CO_2 reaction constant and $\mu_{CO_3^{2-}}$ is the maximum rate of reaction from bicarbonate to CO_3^{2-}.

Appendix B. Identifiability analysis methodology

The initial values of the θ_0 parameters that are necessary to solve the optimization problem were calculated in some cases using the experimental data, the other parameters were taken according to the nature of the phenomenon. One set of experimental data was used for parameter identification and one set for model validation, while different conditions for initial biomass and mercury were used to set model prediction limits for initial biomass and mercury concentrations. The "Simulated Annealing" optimization algorithm was used to solve the parameter estimation problem and obtain an initial pseudo-optimal parameter set θ^*. This parameter set is presented in Table B.1.

The methodology proposed by Yao et al. (2003) is called the "orthogonal method". In this method, the parameters can be estimated if the sensitivity coefficients are not linearly dependent. These coefficients correspond to the derivatives of the state variables x_i with respect to the identifiable parameters θ_k evaluated for each time t_N.

$$Z = \begin{bmatrix} \left.\frac{\partial x_1}{\partial \theta_1}\right|_{t=t_1} & \left.\frac{\partial x_1}{\partial \theta_1}\right|_{t=t_1} & \cdots & \left.\frac{\partial x_1}{\partial \theta_m}\right|_{t=t_1} \\ \left.\frac{\partial x_i}{\partial \theta_1}\right|_{t=t_1} & \left.\frac{\partial x_i}{\partial \theta_1}\right|_{t=t_1} & \cdots & \left.\frac{\partial x_i}{\partial \theta_m}\right|_{t=t_1} \\ \left.\frac{\partial x_1}{\partial \theta_1}\right|_{t=t_2} & \left.\frac{\partial x_1}{\partial \theta_1}\right|_{t=t_2} & \vdots & \left.\frac{\partial x_1}{\partial \theta_m}\right|_{t=t_2} \\ \left.\frac{\partial x_i}{\partial \theta_1}\right|_{t=t_N} & \left.\frac{\partial x_1}{\partial \theta_1}\right|_{t=t_N} & \cdots & \left.\frac{\partial x_i}{\partial \theta_m}\right|_{t=t_N} \end{bmatrix} \tag{B.1}$$

The number of selected θ_k for this analysis cannot be less than the number of state variables x_i. To compare parametric sensitivity coefficients, the sensitivity matrix must be scaled to ensure dimensional consistency. For this, the following equation is used:

$$s_{ij} = z_{ij}\frac{\Delta\theta_j}{SC_i} \tag{B.2}$$

In equation 20, z_{ij} was evaluated at θ^*, the point in the parameter space where the sensitivity analysis is fulfilled, $\Delta\theta_j$ is a scaling factor that reflects the uncertainties associated with the measurements. The sensitivity matrix was scaled using $\Delta\theta_j = 0.5$ according to Brun et al. (2001) and Villegas et al. (2017) because the values used in the present work are the first reported for microalgae cultures. The value of SC_i was defined as the mean value of the output variables. Subsequently, the method applies sequential orthogonal projections to the column vectors of the standardized sensitivity matrix to select one identifiable parameter at a time.

The final results of the parameter identifiability analysis indicate that the most sensitive and linearly independent parameter subgroup is a four-parameter subgroup corresponding to parameters 3, 4, 8, and 14 according to the nomenclature presented in Table B.1.. The determinant DET and the minimum error MSE_Y found for this subgroup are 3.63×10^{-6} and 0.1186, respectively. Table B.2. shows the results of the optimal parameter set $\{\widetilde{\theta} = \theta_k^* \cup \theta_{Fixed}\}$.

Table B1
Pseudo-optimal and initial parameters.

Parameter number	Symbol	Units	Initial Parameter Value θ_0	Pseudo-optimal initial set θ^*
1	μ_{max}	day^{-1}	0.4514	0.333554
2	e_p	mg X^{-1} μm^{-1} L	0.0234	7.9948×10^{-5}
3	k_C	mg C L^{-1}	0.7197	1.2126×10^{-3}
4	$y_{x/c}$	mg X mg C^{-1}	0.6495	3.8099×10^{-2}
5	k_N	mg N L^{-1}	56.6700	49.0045
6	$y_{x/N}$	mg X mg N^{-1}	0.3003	0.2793
7	k_P	mg P L^{-1}	64.8600	54.0097
8	$y_{x/P}$	mg X mg P^{-1}	4.5640	2.0803
9	k_I	μmol m^{-2} s^{-1}	1.1050	6.6436
10	k_{Hg}	mg Hg L^{-1}	0.3770	0.1480
11	k_{Inh}	mg Hg L^{-1}	0.7711	0.2484
12	k_{LaO}	day^{-1}	0.5629	0.5677
13	O_{sat}	mg O L^{-1}	1.6810	3.9933
14	$y_{x/O}$	mg X mg O^{-1}	36.4300	67.7095
15	$v_{max,cw}$	mg Hg L^{-1} day^{-1}	0.3631	0.4238
16	k_{cw}	mg Hg L^{-1}	0.2464	0.1684
17	$v_{max,rev}$	mg Hg L^{-1} day^{-1}	0.5991	0.8950
18	k_{rev}	mg Hg L^{-1}	0.5380	0.3560
19	$v_{max,m1c}$	mg C L^{-1} day^{-1}	0.9996	0.5069
20	k_{m1c}	mg C L^{-1}	0.0036738	0.4393
21	$v_{max,m2c}$	mg C L^{-1} day^{-1}	0.9997	1.4931×10^{-4}
22	k_{m2c}	mg C L^{-1}	0.0029916	0.1138
23	$v_{max,m1n}$	mg N L^{-1} day^{-1}	0.3002	5.7519×10^{-2}
24	k_{m1n}	mg N L^{-1}	0.8242	0.6911
25	$v_{max,m2n}$	mg N L^{-1} day^{-1}	0.1708	0.5254
26	k_{m2n}	mg N L^{-1}	0.7751	0.2407
27	$v_{max,m1p}$	mg P L^{-1} day^{-1}	0.2156	0.2158
28	k_{m1p}	mg P L^{-1}	0.5255	0.5255
29	$v_{max,m2p}$	mg P L^{-1} day^{-1}	0.5761	0.9740
30	k_{m2p}	mg P L^{-1}	0.8242	0.8242
31	$v_{max,m1Hg}$	mg Hg L^{-1} day^{-1}	0.2494	0.8834
32	k_{m1Hg}	mg Hg L^{-1}	0.1633	0.5452
33	$v_{max,m2Hg}$	mg Hg L^{-1} day^{-1}	0.7486	0.9992
34	k_{m2Hg}	mg Hg L^{-1}	0.8034	0.4636
35	k_{infc}	day^{-1}	0.9994	0.5077
36	k_{effc}	day^{-1}	0.9655	0.6067
37	k_{infn}	day^{-1}	0.00187	0.6737
38	k_{effn}	day^{-1}	0.2115	1.0000
39	k_{infp}	day^{-1}	0.3792	0.9278
40	k_{effp}	day^{-1}	0.1414	0.2017
41	k_{infHg}	day^{-1}	0.2986	0.9797
42	k_{effHg}	day^{-1}	0.2427	0.9325
43	k_{Z_C}	day^{-1}	0.0117	5.7024×10^{-2}
44	k_{Z_N}	day^{-1}	0.3810	0.5943
45	k_{Z_P}	day^{-1}	0.1136	1.6891×10^{-2}
46	$k_{Z_{Hg}}$	day^{-1}	0.5215	0.0468
47	v_{max,CO_2}	mg C L^{-1} day^{-1}	0.9842	0.9842
48	k_{CO_2}	mg C L^{-1}	0.2163	0.2159
49	$\mu_{CO_3^{2-}}$	mg C L^{-1} day^{-1}	0.5400	0.8079

Table B2
Identifiable parameters $\boldsymbol{\theta}_{\mathbf{k}}$, fixed $\boldsymbol{\theta}_{\mathbf{Fixed}}$ and optimal $\widetilde{\theta}$.

Parameter number	Symbol	Parameters value subset $\boldsymbol{\theta}_{\mathbf{k}}$	Parameters value subset $\boldsymbol{\theta}_{\mathbf{Fixed}}$	Parameters value Final set $\widetilde{\theta}$
1	μ_{max}	0.3508		0.3508
2	e_p	7.9927×10^{-5}		7.9927×10^{-5}
3	k_C	1.2126×10^{-3}		1.2126×10^{-3}
4	$y_{x/c}$	2.6604×10^{-2}		2.6604×10^{-2}
5	k_N	48.8880		48.8880
6	$y_{x/N}$	0.2772		0.2772
7	k_P	53.8900		53.8900
8	$y_{x/P}$	2.0660		2.0660
9	k_I	6.6450		6.6450
10	k_{Hg}	0.1483		0.1483
11	k_{Inh}	0.2491		0.2491
12	k_{LaO}	0.5677		0.5677
13	O_{sat}	3.9850		3.9850
14	$y_{x/O}$	67.8600		67.8600
15	$v_{max,cw}$		0.4231	0.4231
16	k_{cw}		0.1902	0.1902
17	$v_{max,rev}$		0.8960	0.8960
18	k_{rev}		0.3564	0.3564
19	$v_{max,mac}$		0.5069	0.5069
20	k_{mac}		0.4393	0.4393
21	$v_{max,mbc}$		1.5099×10^{-4}	1.5099×10^{-4}
22	k_{mbc}		0.1138	0.1138
23	$v_{max,man}$		5.7499×10^{-2}	5.7499×10^{-2}
24	k_{man}		0.6911	0.6911
25	$v_{max,mbn}$		0.5252	0.5252
26	k_{mbn}		0.2407	0.2407
27	$v_{max,map}$		0.2157	0.2157
28	k_{map}		0.5255	0.5255
29	$v_{max,mbp}$		0.9737	0.9737
30	k_{mbp}		0.8242	0.8242
31	$v_{max,maHg}$		0.8832	0.8832
32	k_{maHg}		0.5486	0.5486
33	$v_{max,mbHg}$		0.9992	0.9992
34	k_{mbHg}		0.4671	0.4671
35	k_{infc}		0.5077	0.5077
36	k_{effc}	0.6067		0.6067
37	k_{infn}		0.6738	0.6738
38	k_{effn}		1.0000	1.0000
39	k_{infp}		0.9273	0.9273
40	k_{effp}		0.2013	0.2013
41	k_{infHg}		0.9402	0.9402
42	k_{effHg}		1.0000	1.0000
43	k_{Z_C}		5.7024×10^{-2}	5.7024×10^{-2}
44	k_{Z_N}		0.5943	0.5943
45	k_{Z_P}		1.7301×10^{-2}	1.7301×10^{-2}
46	$k_{Z_{Hg}}$		0.1645	0.1645
47	v_{max,CO_2}	0.9842		0.9842
48	k_{CO_2}	0.2155		0.2155
49	$\mu_{CO_3^{2-}}$	0.8070		0.8070

References

Balzano, S., Sardo, A., Blasio, M., Chahine, T.B., Dell'Anno, F., Sansone, C., Brunet, C., 2020. Microalgal metallothioneins and phytochelatins and their potential use in bioremediation. Front. Microbiol. 11, 1–16. https://doi.org/10.3389/fmicb.2020.00517.

Barón-Sola, Á., Toledo-Basantes, M., Arana-Gandía, M., Martínez, F., Ortega-Villasante, C., Dučić, T., Yousef, I., Hernández, L.E., 2021. Synchrotron radiation-fourier transformed infrared microspectroscopy (μSR-FTIR) reveals multiple metabolism alterations in microalgae induced by cadmium and mercury. J. Hazard. Mater. 419 https://doi.org/10.1016/j.jhazmat.2021.126502.

Beauvais-Flück, R., Slaveykova, V.I., Cosio, C., 2018. Molecular effects of inorganic and methyl mercury in aquatic primary producers: comparing impact to a macrophyte and a green microalga in controlled conditions. Geosciences 8. https://doi.org/10.3390/geosciences8110393.

Beauvais-Flück, R., Slaveykova, V.I., Cosio, C., 2017. Cellular toxicity pathways of inorganic and methyl mercury in the green microalga Chlamydomonas reinhardtii. Sci. Rep. 7, 1–12. https://doi.org/10.1038/s41598-017-08515-8.

Beauvais-Flück, R., Slaveykova, V.I., Cosio, C., 2016. Transcriptomic and physiological responses of the green microalga chlamydomonas reinhardtii during short-term exposure to subnanomolar methylmercury concentrations. Environ. Sci. Technol. 50, 7126–7134. https://doi.org/10.1021/acs.est.6b00403.

Blaby-Haas, C.E., Merchant, S.S., 2012. The ins and outs of algal metal transport. Biochim. Biophys. Acta Mol. Cell Res. 1823, 1531–1552. https://doi.org/10.1016/j.bbamcr.2012.04.010.

Borowitzka, M.A., Beardall, J., Raven, J.A., 2016. The Physiology of Microalgae, 1st ed. Springer International Publishing, Cham Switzerland. https://doi.org/10.1007/978-3-319-24945-2. ed.

Brun, R., Reichert, P., Künsch, H.R., 2001. Practical identifiability analysis of large environmental simulation models. Water Resour. Res. 37, 1015–1030. https://doi.org/10.1029/2000WR900350.

Capolino, E., Tredici, M., Pepi, M., Baldi, F., 1997. Tolerance to mercury chloride in Scenedesmus strains. BioMetals 10, 85–94. https://doi.org/10.1023/A:1018375005791.

Chung, T.Y., Kuo, C.Y., Lin, W.J., Wang, W.L., Chou, J.Y., 2018. Indole-3-acetic-acid-induced phenotypic plasticity in Desmodesmus algae. Sci. Rep. 8, 1–13. https://doi.org/10.1038/s41598-018-28627-z.

Cossart, T., Garcia-Calleja, J., Santos, J.P., Kalahroodi, E.L., Worms, I.A.M., Pedrero, Z., Amouroux, D., Slaveykova, V.I., 2022. Role of phytoplankton in aquatic mercury speciation and transformations. Environ. Chem. 19, 104–115. https://doi.org/10.1071/EN22045.

do Nascimento, F.H., Rigobello-Masini, M., Domingos, R.F., Pinheiro, J.P., Masini, J.C., 2017. Dynamic interactions of Hg(II) with the surface of green microalgae Chlamydomonas reinhardtii studied by stripping chronopotentiometry. Algal Res. 24, 347–353. https://doi.org/10.1016/j.algal.2017.04.027.

Duval, J.F.L., 2013. Dynamics of metal uptake by charged biointerphases: bioavailability and bulk depletion. Phys. Chem. Chem. Phys. 15, 7873–7888. https://doi.org/10.1039/c3cp00002h.

Duval, J.F.L., Paquet, N., Lavoie, M., Fortin, C., 2015. Dynamics of metal partitioning at the cell-solution interface: implications for toxicity assessment under growth-inhibiting conditions. Environ. Sci. Technol. 49, 6625–6636. https://doi.org/10.1021/acs.est.5b00594.

Duval, J.F.L., Rotureau, E., 2014. Dynamics of metal uptake by charged soft biointerphases: impacts of depletion, internalisation, adsorption and excretion. Phys. Chem. Chem. Phys. 16, 7401–7416. https://doi.org/10.1039/c4cp00210e.

Fawzy, M.A., Hifney, A.F., Adam, M.S., Al-Badaani, A.A., 2020. Biosorption of cobalt and its effect on growth and metabolites of Synechocystis pevalekii and Scenedesmus bernardii: isothermal analysis. Environ. Technol. Innov. 19, 100953 https://doi.org/10.1016/j.eti.2020.100953.

Furuhashi, K., Saga, K., Okada, S., Imou, K., 2013. Seawater-cultured botryococcus braunii for efficient hydrocarbon extraction. PLoS ONE 8, e66483. https://doi.org/10.1371/journal.pone.0066483.

Galceran, J., Monné, J., Puy, J., Van Leeuwen, H.P., 2006. Transient biouptake flux and accumulation by microorganisms: the case of two types of sites with Langmuir adsorption. Mar. Chem. 99, 162–176. https://doi.org/10.1016/j.marchem.2005.06.006.

Ge, Y., Liu, X., Nan, F., Liu, Q., Lv, J., Feng, J., Xie, S., 2022. Toxicological effects of mercuric chloride exposure on scenedesmus quadricauda. Water 14. https://doi.org/10.3390/w14203228 (Switzerland).

Hajdu, R., Pinheiro, J.P., Galceran, J., Slaveykova, V.I., 2010. Modeling of Cd uptake and efflux kinetics in metal-resistant bacterium cupriavidus metallidurans. Environ. Sci. Technol. 44, 4597–4602. https://doi.org/10.1021/es100687h.

Hussain, F., Eom, H., Ali Toor, U., Lee, C.S., Oh, S.E., 2020. Rapid assessment of heavy metal-induced toxicity in water using micro-algal bioassay based on photosynthetic oxygen evolution. Environ. Eng. Res. 26 https://doi.org/10.4491/eer.2020.391, 200391–0.

Ibuot, A., Dean, A.P., Pittman, J.K., 2020. Multi-genomic analysis of the cation diffusion facilitator transporters from algae. Metallomics 12, 617–630. https://doi.org/10.1039/d0mt00009d.

León-Vaz, A., Romero, L.C., Gotor, C., León, R., Vigara, J., 2021. Effect of cadmium in the microalga Chlorella sorokiniana: a proteomic study. Ecotoxicol. Environ. Saf. 207 https://doi.org/10.1016/j.ecoenv.2020.111301.

Li, Y.Y., Li, D., Song, B., Li, Y.Y., 2022. The potential of mercury methylation and demethylation by 15 species of marine microalgae. Water Res. 215, 118266 https://doi.org/10.1016/j.watres.2022.118266.

Liu, M., Zhang, Q., Maavara, T., Liu, S., Wang, X., Raymond, P.A., 2021. Rivers as the largest source of mercury to coastal oceans worldwide. Nat. Geosci. 14, 672–677. https://doi.org/10.1038/s41561-021-00793-2.

Ma, J.F., Ryan, P.R., Delhaize, E., 2001. Aluminium tolerance in plants and the complexing role of organic acids. Trends Plant Sci. 6, 273–278. https://doi.org/10.1016/S1360-1385(01)01961-6.

Palomino, F., Asistente, P., , Unidad de Fisiología, Rojas, M., Ocasional, D., Unidad de Toxicología, 1997. Nueva técnica colorimétrica para la determinación de nitratos en el plasma. Rev. Fac. Med. Univ. Nac. Colomb. 45 (2), 63–69.

Piotrowska-Niczyporuk, A., Bajguz, A., Zambrzycka-Szelewa, E., 2017. Response and the detoxification strategies of green alga Acutodesmus obliquus (Chlorophyceae) under lead stress. Environ. Exp. Bot. 144, 25–36. https://doi.org/10.1016/j.envexpbot.2017.08.013.

Pokora, W., Baścik-Remisiewicz, A., Tukaj, S., Kalinowska, R., Pawlik-Skowrońska, B., Dziadziuszko, M., Tukaj, Z., 2014. Adaptation strategies of two closely related *Desmodesmus armatus* (green alga) strains contained different amounts of cadmium: a study with light-induced synchronized cultures of algae. J. Plant Physiol. 171, 69–77. https://doi.org/10.1016/j.jplph.2013.10.006.

Pradhan, B., Bhuyan, P.P., Nayak, R., Patra, S., Behera, C., Ki, J., Ragusa, A., Lukatkin, A. S., Jena, M., 2022. Microalgal phycoremediation: a glimpse into a sustainable environment. Toxics 10, 1–16.

Présent, R.M., Rotureau, E., Billard, P., Pagnout, C., Sohm, B., Flayac, J., Gley, R., Pinheiro, J.P., Duval, J.F.L., 2017. Impact of intracellular metallothionein on metal biouptake and partitioning dynamics at bacterial interfaces. Phys. Chem. Chem. Phys. 19, 29114–29124. https://doi.org/10.1039/c7cp05456d.

Priyadarshanee, M., Chatterjee, S., Rath, S., Dash, H.R., Das, S., 2022. Cellular and genetic mechanism of bacterial mercury resistance and their role in biogeochemistry and bioremediation. J. Hazard. Mater. 423, 126985 https://doi.org/10.1016/j.jhazmat.2021.126985.

Roger, B., Bridgewater, L., 2017. Standard Methods for the Examination of Water and Wastewater, 23rd ed. American Public Health Association (APHA), Washington, D.C.

Rotureau, E., Billard, P., Duval, J.F.L., 2015. Evaluation of metal biouptake from the analysis of bulk metal depletion kinetics at various cell concentrations: theory and application. Environ. Sci. Technol. 49, 990–998. https://doi.org/10.1021/es505049f.

Spain, O., Plöhn, M., Funk, C., 2021. The cell wall of green microalgae and its role in heavy metal removal. Physiol. Plant. 173, 526–535. https://doi.org/10.1111/ppl.13405.

Tijani, H., Yuzir, A., Dagang, W.R.Z.W., Zamyadi, A., Abdullah, N., 2018. Multi-parametric modelling and kinetic sensitivity of microalgal cells. Algal Res. 32, 259–269. https://doi.org/10.1016/j.algal.2018.04.009.

Tramontin, D.P., Gressler, P.D., Rörig, L.R., Derner, R.B., Pereira-Filho, J., Radetski, C. M., Quadri, M.B., 2018. Growth modeling of the green microalga Scenedesmus obliquus in a hybrid photobioreactor as a practical tool to understand both physical and biochemical phenomena in play during algae cultivation. Biotechnol. Bioeng. 115, 965–977. https://doi.org/10.1002/bit.26510.

Tripathi, S., Poluri, K.M., 2021. Heavy metal detoxification mechanisms by microalgae: insights from transcriptomics analysis. Environ. Pollut. 285, 117443 https://doi.org/10.1016/j.envpol.2021.117443.

Umetani, I., Janka, E., Sposób, M., Hulatt, C.J., Kleiven, S., Bakke, R., 2021. Bicarbonate for microalgae cultivation: a case study in a chlorophyte, Tetradesmus wisconsinensis isolated from a Norwegian lake. J. Appl. Phycol. 33, 1341–1352. https://doi.org/10.1007/s10811-021-02420-4.

Vendruscolo, R.G., Fagundes, M.B., Maroneze, M.M., do Nascimento, T.C., de Menezes, C.R., Barin, J.S., Zepka, L.Q., Jacob-Lopes, E., Wagner, R., 2019. Scenedesmus obliquus metabolomics: effect of photoperiods and cell growth phases. Bioprocess Biosyst. Eng. 42, 727–739. https://doi.org/10.1007/s00449-019-02076-y.

Villegas, A., Arias, J.P., Aragón, D., Ochoa, S., Arias, M., Aragï¿½n, D., Ochoa, S., Arias, M., 2017. Structured model and parameter estimation in plant cell cultures of Thevetia peruviana. Bioprocess Biosyst. Eng. 40, 573–587. https://doi.org/10.1007/s00449-016-1722-6.

Yan, A., Wang, Y., Tan, S.N., Yusof, M.L.M., Gosh, S., Chen, Z., 2020. Phytoremediation : a promising approach for revegetation of heavy-polluted land. Front. Plant Sci. 11, 1–15. https://doi.org/10.3389/fpls.2020.00359.

Yao, K.Z., Shaw, B.M., Kou, B., McAuley, K.B., Bacon, D.W., 2003. Modeling ethylene/butene copolymerization with multi-site catalysts: parameter estimability and experimental design. Polym. React. Eng. 11, 563–588. https://doi.org/10.1081/PRE-120024426.